Journal Name

ARTICLE

A velocity map imaging study of the photodissociation of the methyl iodide cation

Received 00th January 20xx,
Accepted 00th January 20xx

DOI: 10.1039/x0xx00000x

www.rsc.org/

S. Marggi Poullain[a], D. V. Chicharro[a], J. González-Vázquez[b], L. Rubio-Lago[a] and L. Bañares[a]

The photodissociation dynamics of the methyl iodide cation has been studied using the velocity map imaging technique. A first laser pulse is used to ionize methyl iodide via a (2+1) REMPI scheme through the 5$p\pi \rightarrow$ 6p Rydberg state two-photon transition. The produced CH_3I^+($\tilde{X}\,^2E_{3/2}$) ions are subsequently excited at several wavelengths between 242 and 260 nm. The reported translational energy distributions for the methyl and iodine ions present a Boltzmann-type unstructured distribution at low excitation energies as well as a recoiled narrow structure at higher excitation energies highlighting two different dissociation processes. High level *ab initio* calculations have been performed in order to get a deeper understanding of the photodissociation dynamics of the CH_3I^+ ion. Direct dissociation on a repulsive state from the manifold of states representing the $\tilde{B}$ excited state leads to CH_3^+($\tilde{X}\,^1A_1'$) + I*($^2P_{1/2}$), while the $CH_3 + I^+(^3P_2)$ channel is populated through an avoided crossing outside the Franck Condon region. On the contrary, an indirect process involving a transfer of energy from highly excited electronic states to the ground state of the ion is responsible of the observed Boltzmann-type distributions.

Introduction

Methyl iodide (CH_3I) has been a benchmark system for the study of photoinduced molecular dynamics for the past two decades. In particular, the photodissociation in the first and second absorption bands has been largely reported and revisited [1–5]. This molecule has also proven to be an excellent system for the demonstration of new experimental techniques, such as ion imaging by Chandler and Houston[6] or the velocity map imaging (VMI) by Eppink and Parker[7]. Studies on the methyl iodide cation (CH_3I^+) are, on the other hand, quite limited. Published literature includes, in particular, photoelectron spectra using first a Helium lamp[8,9] and lately synchrotron radiation[10]; high-resolution spectra for the $\tilde{A}\,^2A_1 \leftarrow \tilde{X}\,^2E_{3/2}$ transition recorded using mass-analyzed threshold ionization[11–13], which provided information about the ro-vibrational structure of the ground ($\tilde{X}\,^2E_{3/2}$) and first excited ($\tilde{A}\,^2A_1$) states and a detailed investigation of the Jahn-Teller effect in the $\tilde{X}\,^2E$ ground state[14]. Some theoretical work has also been reported regarding the position of different electronic states of the ion. The most recent work includes a schematic representation of the potential energy surfaces based on *ab initio* calculations by Locht *et al.*[15]

The ground electronic state of the CH_3I^+ ion is a bound state split into two spin-orbit compounds ($^2E_{3/2}$ and $^2E_{1/2}$) lying at 9.53 eV and 10.15 eV [8,15], respectively, which correlates to the CH_3^+($\tilde{X}\,^1A_1'$) + I($^2P_{3/2}$) dissociation limit at 12.18 eV[16]. The first excited state, $\tilde{A}\,^2A_1$ is a slightly bound state located at around 12.5 eV with respect to the CH_3I ground state while the second excited state, $\tilde{B}\,^2E$, is a pure dissociative state located between 14 and 16 eV [10]. To the best of our knowledge, there are no reported studies on the photodissociation dynamics of the methyl iodide cation through the first and second excited states.

Some studies have been published on the photodissociation dynamics of other alkyl halides cations[17–21]. Aguirre and Pratt[17,18] reported a detailed velocity map imaging study of the one-photon dissociation of CF_3I^+ ions produced by resonance enhanced multiphoton ionization. Photoelectron spectra were measured to characterize the parent ion produced in the $\tilde{X}\,^2E_{3/2}$ ground state, while ion translational energy distributions for the CF_3^+ and I^+ ions produced following excitation to the first excited state of the CF_3I^+ ion, the $\tilde{A}\,^2A_1$ state, were obtained as a function of the dissociation wavelength. For both CF_3^+ + I, and CF_3 + I^+ channels, two different mechanisms were observed. The first corresponds to the direct and fast dissociation of the $\tilde{A}\,^2A_1$ state resulting in high translational energies. The second mechanism, appearing at low translational energies, was described by the internal energy distribution of the nascent fragment. The CF_3^+ + I channel was found to be characterized by a high vibrational excitation in the ν_2 umbrella mode of the molecular ion fragment, that can

[a] Departamento de Química Física I, Facultad de Ciencias Químicas, Universidad Complutense de Madrid, 28040 Madrid, Spain
[b] Departamento de Química, Módulo 13, Facultad de Ciencias, Universidad Autónoma de Madrid, 28049 Madrid, Spain

† Footnotes relating to the title and/or authors should appear here.
Electronic Supplementary Information (ESI) available: [details of any supplementary information available should be included here]. See DOI: 10.1039/x0xx00000x

be understood by considering the Franck–Condon factors between the pyramidal CF_3 moiety in CF_3I^+ and the planar CF_3^+ cation.

In addition, Blanchet *et al.*[19] and Wang *et al.*[20] published almost simultaneously, studies on the competition between the photodissociation of methyl bromide and methyl bromide cation by slice and velocity map imaging. A series of anisotropic rings characterized by low translational energies were observed for the methyl ion in both studies and assigned to the formation of $CH_3Br^+(\tilde{X}\,^2E_{3/2})$, by either two-photon non-resonant excitation[19] or by using a (2+1) REMPI scheme[20], followed by the one-photon dissociation in the second absorption band ($\tilde{B}\,^2E$ state, in the C_s symmetry group). This process is characterized by a vibrational progression in the ν_2 umbrella mode of the methyl ion suggesting again that the dissociation is controlled by the Franck-Condon factors between the CH_3 moiety in CH_3Br^+ and the CH_3^+ fragment.

Recently, the photofragmentation dynamics of ethyl bromide and ethyl iodide cations were studied using velocity map imaging by Vallance and co-workers[21]. The experimental results were interpreted with the aid of high-level *ab initio* potential energy surfaces. Regarding the C-I bond fission in the $C_2H_5I^+$ photodissociation, translational distributions for the ethyl ion were also found to be bimodal, where the low energy part was associated with near-threshold photodissociation, while the high translational energy region was attributed to the prompt dissociation in the second absorption band ($\sigma\sigma^*$).

The aim of this work is to study the photodynamics of the dissociation of the methyl iodide cation using velocity map imaging. A scheme of the experimental procedure is shown in Figure 1. A first laser pulse is centred at 339.34 nm in order to produce $CH_3I^+(\tilde{X}\,^2E)$ ions through a (2+1) REMPI scheme corresponding to the two-photon excitation of the $5p\pi \leftarrow 6p$ $[2]0_0^0$ Rydberg state[22]. A second laser pulse excited the methyl iodide ion into the first and second, $\tilde{A}\,^2A_1$ and $\tilde{B}\,^2E_1$, excited states. The methyl and iodine ions produced from the photodissociation of the CH_3I^+ are then detected using velocity map imaging. The experimental results, *i.e.* translational energy distribution and angular distributions, are interpreted with the aid of high-level *ab initio* calculations.

The paper is organized as follows: in Section 2 the experimental and theoretical approaches are presented. In Sections 3 the most relevant experimental and theoretical results are presented and discussed, respectively, and, finally, Section 4 is dedicated to present the most important conclusions of the work.

Methods

Experimental

The main characteristics of the experimental setup have been described in detail previously [4]. The whole experiment runs at a repetition rate of 10 Hz. Methyl iodide was seeded in helium (10%, 1 atm backing pressure) and expanded into the vacuum using a pulsed nozzle (General Valve Series 9, 0.5 mm orifice) in order to generate the supersonic beam. The gas pulse passes through a skimmer (Beam Dynamics, Standard Model 2, 0.5 mm diameter orifice) and reaches the ionization chamber where the molecular beam is intersected at right angles, in the middle of the electrical plates of a time-of-flight (TOF) mass spectrometer, by the ionization and the dissociation laser pulses, which are focused (f = 25 cm) and counter propagated to each other.

The second harmonic of a Nd:YAG (Quanta Ray Pro 230) pumped dye laser (Sirah Cobra-Stretch) is used in order to ionize the methyl iodide *via* a (2+1) REMPI scheme at 339.34 nm corresponding to the $5p\pi \leftarrow 6p$ Rydberg state two-photon transition[22]. The CH_3I^+ ions produced are then excited at several wavelengths: 260, 250 and 242 nm using a Nd:YAG (Quanta Ray Pro 190) pumped frequency doubled dye laser (Sirah Cobra-Stretch).

CH_3^+ and I^+ images are recorded using our velocity map imaging (VMI) apparatus in the single-field configuration[23,24]. The generated ions are accelerated by an electric potential of 5 kV applied to the repeller plate and pass through a field-free TOF region (45 cm) before hitting the impedance matched microchannel plates (MCPs, Chevron configuration, 40 mm diameter). The MCPs can be gated with a high voltage pulse to allow only the ions of interest to be detected. The resulting electron avalanche strikes a phosphor screen (P47), thereby creating the ion image, which is recorded by a CCD camera (SONY 1024 x 768 pixel) controlled using National Instruments (NI) LabView 7.1 and IMAQ VISION software. The final image is obtained as the sum of around 20 000–100 000 laser shots, depending on the quality of the signal.

The recorded velocity map methyl or iodine ions images are quadrant symmetrised and Abel inverted using the Hankel transform prior to extracting the kinetic energy spectrum and the angular distribution.

Independent velocity-radius calibration of the apparatus is done by measuring resonantly ionized CH_3 ($\nu = 0$) fragments produced after the photodissociation of CH_3I at 333.45 nm (one colour pump–probe experiment) at different repeller potentials, taking advantage of the well known kinetic energy release of the $I(^2P_{3/2})$ yielding channel at this photolysis wavelength[4].

Theoretical

In order to characterize the methyl iodide cation, the energy of the different electronic states was calculated along the C-I distance. This calculation was performed using multireference methods with relativistic corrections and a ANO-RCC[25,26] basis set contracted to a TZP equivalent with a CASSCF wavefunction that was obtained using 6 electrons on 4 orbitals as depicted in Figure 2. The set of orbitals considered in this study contain

two lone pairs in the iodine atom, the σ bonding and the σ antibonding. These orbitals were optimized using the state average technique where the 12 doublets (7 of symmetry *A*' and 5 of symmetry *A*") and 3 quadruplets (1 of symmetry *A*' and 2 of symmetry *A*") were included. The spin-orbit (SO) was taken into account using the AMFI approximation[27], resulting in a total of 36 electronic states. This number of states is required to describe correctly the dissociation limits of the first six channels (in order of increasing energy): $CH_3^+ + I(^2P_{3/2})$; $CH_3 + I^+(^3P_2)$; $CH_3^+ + I(^2P_{1/2})$; $CH_3 + I^+(^3P_0)$; $CH_3 + I^+(^3P_1)$; $CH_3 + I^+(^1S)$.

The CASSCF energy was corrected by considering single and double excitations from the CASSCF wavefunctions (MRCISD). All the calculations were performed at C_s symmetry with the MOLPRO package [28,29], using the modules SEWARD[30], CASSCF [31,32], the CI[33–36] and geometry optimization[37] with analytical gradients for MP2[38] and CASPT2[39]. In all cases relativistic effects were taken into account by using the Douglas-Kroll Hamiltonian[40–42] and calculating the SO coupling.[43]

Table 1 shows the energy of the electronic states of the methyl iodide cation at two different geometries: the minimum of the neutral molecule obtained at MP2 level; and in the dissociation limit referred to the ground state energy of the neutral. The active space at the equilibrium distance for the neutral is depicted in Figure 2 where the geometry corresponds to C_{3v} symmetry with a C-I distance of 2.133 Å, a C-H distance of 1.077 Å, and a I-C-H angle of 107.6 degrees. In order to calculate the ionization energy, a MRCISD using the same active space and including 4 singlets (3 of symmetry *A*' and 1 of symmetry *A*") and 3 triplets (2 of symmetry *A*' and 1 of symmetry *A*") was calculated for the neutral molecule. The dissociation limit was defined by a restricted optimization (C-I distance of 10 Å) at CASPT2 level (considering only the first three doublets to describe correctly the first ionization limit) in the ground state of the cation, where the cation of the methyl fragment is planar with a C-H distance of 1.068 Å. Since the calculated ionization energy is 9.10 eV and the first dissociation limit is at 12.12 eV, it is not possible to obtain ionization for the first electronic state of the cation. In fact, it is required to excite at least to the fifth electronic state (12.37 eV) to overpass the dissociation energy.

Experimental Results

Figures 3a and 3c present the VMI inverted images recorded for the CH_3^+ and I^+ ions, respectively, in a one-colour experiment using photon excitation at 339.34 nm. A highly anisotropic structure is observed in both cases that can be assigned to a two steps process. First, the ground state CH_3I parent molecule is ionized *via* a (2+1) REMPI scheme; second, the CH_3I^+ cation thus formed is excited and dissociated through further absorption of one additional photon. The three-photon absorption step cannot lead to dissociation, since the total excitation energy (10.96 eV) is lower than the first dissociation limit of the CH_3I^+, which is 12.18 eV for the $CH_3^+(\tilde{X}\,^1A_1') + I(^2P_{3/2})$ channel.

Angular integration of the images shown in Figs. 3a and 3c leads to the total translational energy distributions (TEDs) shown in Fig 3b and 3d, respectively. For both ions, a Boltzmann-type distribution centred at around 0.15 eV is observed. The vertical bars represent the maximum available energy for the $CH_3^+(\tilde{X}\,^1A_1') + I(^2P_{3/2})$ (Figure 3b) and $CH_3(\tilde{X}\,^2A_2'') + I^+(^3P_2)$ (Figure 3d) channels. If we consider photo-ionization into $CH_3I^+(\tilde{X})$ in its ground ro-vibrational state, the available energy will be given by:

$$E_{av} = \left(IP + h\nu\right) - E_D \qquad (1)$$

where $h\nu$ is the excitation photon energy for λ_{exc} (here $\lambda_{exc} = \lambda_{ion}$), E_D is the dissociation energy of CH_3I^+: 12.18 eV and 12.90 eV for the $CH_3^+(\tilde{X}\,^1A_1') + I(^2P_{3/2})$ and $CH_3(\tilde{X}\,^2A_2'') + I^+(^3P_2)$ channels[16], respectively. *IP* represents the ionization potential, here 9.54 and 10.16 eV for $\tilde{X}\,^2E_{3/2}$ and $\tilde{X}\,^2E_{1/2}$, respectively[44]. We note, in addition, that the possible photodissociation of the 6*p* Rydberg state following two-photon absorption at 339.34 nm has been considered and would give rise to structures at higher energies that were not observed in all performed experiments.

The portion of the TED lying at values below the available energy in Figs. 3b and 3d corresponds to fragments produced with internal energy; on the other hand, the portion of the TED at higher energies is associated with fragments produced in the dissociation of internally excited CH_3I^+ ions. Since the CH_3^+ species is detected as is produced, the observed Boltzmann distribution in Fig. 3b indicates a high ro-vibrational excitation of the nascent CH_3^+ ion, a quite usual fact in dissociative multiphoton ionization (MPI) processes. In contrast, Fig. 3d indicates a significant contribution to the $CH_3(\tilde{X}\,^2A_2'') + I^+(^3P_2)$ channel from internally excited CH_3I^+ ions.

Figure 4a represents the VMI inverted image for the CH_3^+ ion produced in a two-colour experiment where the CH_3I^+ cation is firstly produced using three photons at 339.34 nm and the cation subsequently dissociated after excitation with a photon at 260 nm. One colour contributions to the raw image coming from each laser have been carefully subtracted prior inversion. The image presents a low-recoiled highly anisotropic structure, similar to the one observed in Fig. 3a, which denotes a typical dissociative MPI process. However, a weak anisotropic ring with a clear parallel character is observed in this case, which can be attributed to the two colour process*, i. e*. to the one-photon dissociation of CH_3I^+ at 260 nm. The corresponding TED is obtained by angular integration of the image and is shown in the inset of Fig. 4b. The four vertical bars indicate the available energy for the four dissociation channels considered obtained using Eq (1):

$CH_3I^+(\tilde{X}\,^2E_{3/2}) \rightarrow CH_3^+(\tilde{X}\,^1A_1') + I^*(^2P_{1/2})$ (2)

$CH_3I^+(\tilde{X}\,^2E_{3/2}) \rightarrow CH_3^+(\tilde{X}\,^1A_1') + I(^2P_{3/2})$ (3)

$CH_3I^+(\tilde{X}\,^2E_{1/2}) \rightarrow CH_3^+(\tilde{X}\,^1A_1') + I^*(^2P_{1/2})$ (4)

$CH_3I^+(\tilde{X}\,^2E_{1/2}) \rightarrow CH_3^+(\tilde{X}\,^1A_1') + I(^2P_{3/2})$ (5)

Clearly, the observed structure can be assigned to the formation of CH_3^+ ions in correlation with spin-orbit excited iodine atoms, $I^*(^2P_{1/2})$, produced from the dissociation of ground state $CH_3I^+(\tilde{X}\,^2E_{3/2})$. Since the observed peak represents ≈ 4% of the MPI signal located at the centre of the image, in order to investigate the peak profile, the energy region above 0.8 eV, which avoids the MPI feature, has been represented separately in detail in Fig. 4b. The vertical solid line in Fig. 4b represents, therefore, the available energy for the $CH_3^+(\tilde{X}\,^1A_1') + I^*(^2P_{1/2})$ channel. The narrow structure observed is developed towards energies above the channel reference, which indicates that the process involves some vibrational excitation of the $CH_3I^+(\tilde{X}\,^2E_{3/2})$ parent ion. However, the photoelectron spectrum could not be measured in the present experiments and the vibrational distribution in the $CH_3I^+(\tilde{X})$ ion produced by the (2+1) REMPI scheme remains unknown. The maximum of the distribution is expected for ν=0 taking into account the forecast Franck-Condon factors since the geometry of the CH_3I^+ cation is similar to that of the neutral $CH_3I(\tilde{X})$. The broadening characterizing the structure has been tentatively attributed to the C-I stretch mode (ν_3) which is the most plausible vibrational mode taking part in the C-I bond cleavage. The dashed lines in Fig. 4b represent the available energy for CH_3^+ fragment produced in the photodissociation of $CH_3I^+(\tilde{X}\,^2E_{3/2},\nu_3)$ cations. The observed broad peak corresponds to photodissociation of vibrationally excited $CH_3I^+(\tilde{X}\,^2E_{3/2},\nu_3)$ cations between ν_3=0 and 3 with a maximum at ν_3=1. On the other hand, the rapid fall of the distribution towards the left side of the reference indicates that the CH_3^+ fragment is produced in its ground vibrational state. The lack of vibrational excitation in the fragment together with the high anisotropy observed (discussed later), suggests that the narrow ring should be attributed *a priori* to a direct and rapid dissociation process.

The I^+ ion image recorded in the same conditions is presented in Fig. 4c. Only a weak signal is observed at the centre of the image, which may be associated with a dissociative multiphoton ionization process. Although the pump and probe signals are significantly low in this case, the contribution of each laser alone has been carefully subtracted. The vertical bar represents the maximum available energy for one-photon dissociation at 260 nm of $CH_3I^+(\tilde{X}\,^2E_{3/2})$ giving rise to $CH_3(\tilde{X}\,^2A_2'') + I^+(^3P_2)$ products. The TED is qualitatively similar to the one observed at 339.34 nm, involving an important ro-vibrational excitation of the CH_3 radical co-fragment. In contrast to the CH_3^+ ion image (Fig. 4a) no other feature is observed, although from an energetic point of view, the photon energy would permit to excite the CH_3I^+ to the second $\tilde{B}$ absorption band and then dissociate into $CH_3(\tilde{X}\,^2A_2'') + I^+(^3P_2)$. Thus, at this photon energy the I^+ ion channel could require to overcome an energetic barrier or to populate an upper excited state.

The inverted images for CH_3^+ and I^+ ions from the CH_3I^+ cation photodissociation at 250 nm are depicted in Figs. 5a and 5b, respectively. One colour contributions to the raw image coming from each laser have been carefully subtracted prior inversion. Similarly to Fig. 4a, the CH_3^+ image presents a strong anisotropic broad structure in the centre and weaker anisotropic rings with parallel character. Analogous structures are observed in this case in the I^+ image (Fig. 5c) with an outer broad anisotropic ring with parallel character. The anisotropic structure in the centre is in both cases associated with a dissociative MPI process characterized by a strong ro-vibrational excitation of the fragment detected or, in the case of the I^+ ion, the CH_3 co-fragment. Like in the one colour 339.34 nm experiment, a Boltzmann distribution is measured for the MPI contribution for the two colour experiments. Its characteristics do not vary indeed with the dissociation photon wavelength.

Figures 5b and 5d show the TEDs corresponding to the CH_3^+ and I^+ images. The corresponding energy regions where the observed rings appear are shown in detail. The patterns observed for the dissociation of the CH_3I^+ into CH_3^+ at 260 nm (see Fig. 4b) are reproduced here at 250 nm. First, the anisotropic ring can be attributed to the formation of CH_3^+ ions in correlation with $I^*(^2P_{1/2})$ atoms. Second, the CH_3^+ fragments are produced internally cold, but from vibrationally excited $CH_3I^+(\tilde{X}\,^2E_{3/2})$ parent ions. According to the limits for vibrational excitation of the CH_3I^+ in the ν_3 mode (represented by dashed lines in Fig. 5b), the CH_3^+ ion TED shows a maximum for $\nu_3 = 0$ and 1 and a shoulder for $\nu_3 = 2$, similarly to the results obtained at 260 nm. In contrast with the results at 260 nm, the TED obtained of the I^+ ion at 250 nm shows a broader and unstructured peak at around 1.6 eV (corresponding to the ring with parallel character observe in the image of Fig. 5c), which is characterized by a full-width-half-maximum (FWHM) of ≈0.3 eV. As in the case of the CH_3^+ ion, the structure is associated to the dissociation of vibrationally excited CH_3I^+ ions, and is tentatively assigned to vibrational activity in the ν_3 mode.

Figures 6a to 6c show the results for the photodissociation of CH_3I^+ cation at 242 nm yielding CH_3^+ and I^+ ions. Similar results to those obtained at 250 nm are found in this case for both photofragments: an unstructured strong anisotropic signal in the centre of the image and anisotropic rings with parallel character. Despite the lack of resolution in the associated TEDs (shown in Figs. 6b and 6d), the anisotropic rings can be attributed to dissociation of internally excited $CH_3I^+(\tilde{X}\,^2E_{3/2})$ cations. The vertical bars which mark the available energy indicate that a non-inverted distribution in ν_3 of $CH_3I^+(\tilde{X}\,^2E_{3/2},\nu_3)$ molecules are responsible for the production of CH_3^+ ions, while a small inversion around ν_3 = 1-2 is expected for the I^+ ion. In fact, at 250 and 242 nm – the wavelengths at which an anisotropic ring is observed for the I^+ channel – the FWHM of the recoiled structures reflects a stronger vibrational excitation of the parent CH_3I^+ compared to that of the CH_3^+ ion channel (≈0.5 eV for the I^+ and ≈0.1 eV for the CH_3^+). For both dissociation channels, the FWHM does not show a dependence on the excitation energy.

The branching ratio of the recoiled peak with respect to the MPI signal at the centre of the image increases with the dissociation photon energy in both cases. For the CH_3^+ channel, the recoiled peak increases from 4 % of the MPI signal at 260 nm to ≈25 % at 242 nm; for the I^+ channel, the recoiled contribution represents ≈7% of the MPI signal at 250 nm and 12% at 242 nm. It is important to mention that the displacement in energy of the recoiled peak observed for both I^+ and CH_3^+ ion channels as a function of the excitation photon wavelength confirms a one-photon dissociation process of the CH_3I^+($\tilde{X}\,^2E_{3/2}$) ion.

The angular distributions for the CH_3^+ ion obtained by radial integration of the images depicted in Figs. 3a, 4a, 5a and 6a are presented in Figure 7. The angular distribution shown in Fig. 7a corresponds to the broad low-recoiled anisotropic structure measured at 339.34 nm, while for 260, 250 and 242 nm, the angular distributions correspond to the anisotropic ring with parallel character. All angular distributions show a similar strong alignment along the laser polarization axis (parallel distributions) and are fitted using:

$$I(\theta) \propto \sum_{k=1}^{n} \beta_{2k} P_{2k}\left(\cos\theta\right) \qquad (6)$$

where θ is the angle between the photofragment recoil velocity and the photolysis laser polarization direction; *n* is the number of absorbed photons, β_{2k} are the anisotropy parameters and P_{2k} represent the Legendre polynomials. We note that it is necessary to take into account all the absorbed photons from both the ionization laser and the dissociation laser, so that *n* = 4 for the main process studied here (3 for the one colour experiment). Up to four anisotropy parameters could be needed, therefore, to characterize the angular distribution. The obtained β anisotropy parameters are summarized in Table 2. For all wavelengths, the angular distributions for the CH_3^+ ion are characterized by two anisotropy parameters, with values $\beta_2 \approx 1.6$ and $\beta_4 \approx -0.4$ for the narrow structure. The obtained parameters are in agreement with a first two-photon transition to the 6*p* Rydberg state characterized by a parallel orientation of the C-I bond with respect to the polarization axis. The first three-photon transition generates an ensemble of CH_3I^+ ions with the internuclear C-I axis aligned along the polarization axis, the X axis. Since in the XX polarization configuration, as used in this work, both pulses are polarized along the same axis, the dissociation pulse would, therefore, favour transitions along the C-I bond. In other words, if the dissociation takes place through a parallel transition, the process would be enhanced and high β_2 parameters are expected. A deeper interpretation of the angular distributions cannot be performed at this level. Considering *n* photons, the ion angular distribution for a dissociation process results from the *n* bound-to-bound transitions while for a dissociative ionization process, such as those reported here, this angular distribution can be described as the result of the (*n*-1) bound-to-bound transitions between valence states plus the effect of the photoionization reaction. A modelization of the angular distribution taking into account the 2-photon transition in the REMPI scheme as well as the photoionization reaction (through the dipole matrix elements) and the last bound-to-bound transition from the CH_3I^+ ($\tilde{X}\,^2E_{3/2}$) could help to extract the whole information on the reaction pathway[45,46].

Figure 8 represents the angular distributions for the I^+ channel obtained through angular radial integration of the images shown in Figs. 3c, 5c and 6c. The angular distribution shown in Fig. 8a corresponds to the broad, low-recoiled anisotropic structure measured at 339.34 nm, while for 250 and 242 nm, the angular distributions correspond to the anisotropic rings. All distributions are strongly anisotropic, reflecting an important alignment of the molecule along the polarization axis of the ionizing pulse. Three β asymmetry parameters are required to characterize these distributions using eq (6). In particular, β_2 values above 2 have been found for the anisotropic ring at 250 and 242 nm.

Theoretical Results

Potential energy surfaces (PESs) of the first electronic states of CH_3I^+ in the C_s symmetry group along the C-I dissociative coordinate were calculated and are presented in Figures 9 and 10. In Fig. 9, the methyl moiety is considered to have a rigid pyramidal geometry in all calculated states. The calculations performed without taking into account the spin-orbit coupling, shown in Fig. 9a, provide information about the symmetry of the electronic states involved. In agreement with the measured HeI photoelectron spectra previously reported[8,10], the CH_3I^+ cation presents a bound ground state and a slightly bound first excited state followed by a manifold of purely repulsive states associated with the second absorption $\tilde{B}$ band.

The ^2E ground electronic state in the C_{3v} symmetry group corresponds to a combination of $^2A'$ and $^2A''$ states in the C_s symmetry group as it can be observed in the figure. Similarly, the $\tilde{A}\,^2A_1$ first excited state in C_{3v} becomes a $^2A'$ state in C_s. In the literature, the $\tilde{B}$ second electronically excited state located between 4.5 and 6.5 eV with respect to the CH_3I^+($\tilde{X}\,^2E$) ground state is identified as a $\tilde{B}\,^2E$ state corresponding to $^2A' + {}^2A''$ states in the C_s symmetry group[15]. However, in the present calculations, the manifold of repulsive states accessible through vertical transitions from the ground state at ≈5 eV is composed of $^4A''$, $^4A'$ and $^2A''$ electronic states followed by several $^2A'$ and $^2A''$ states at higher energies. The computed PESs shown here in Fig. 9a are in relative good agreement with the ones reported recently by Vallance and co-workers[21] for the ethyl iodide cation.

In contrast to the PESs shown in Fig. 9a, the computed PESs taking into account the spin-orbit coupling depicted in Fig. 9b do not allow us to identify the symmetry of the different electronic states but represent more accurate dissociation limits. The degeneracy of the electronic states disappears and a more complex picture arises. The ground electronic state is split into two spin-orbit compounds: $^2E_{3/2}$ and $^2E_{1/2}$. The slightly

bound first electronic state is clearly identified around 2.75 eV in the Franck-Condon region associated with the ground state $CH_3I^+(\tilde{X}\,^2E)$ and correlates to the $CH_3 + I^+(^3P_2)$ channel, which appears as the first dissociation limit. At higher energies, the complexity of the repulsive states manifold is considerably enhanced.

As mentioned above, the photodissociation of methyl halide cations is governed by the geometry change of the methyl moiety between the molecular ion (pyramidal) and the radical (planar). Figure 10 presents, therefore, the PESs computed taking into account such relaxation of the methyl geometry, first without the spin-orbit coupling (Fig. 10a) and second including it (Fig. 10b). The geometry relaxation does not alter the symmetry of the electronic states (Figs. 9a and 10a), but the order of the different states varies considerably, especially outside the Franck-Condon region. The most remarkable result is associated with the differences in the potential energy of the fragments at long C-I distances (dissociation limits) as summarized in Table 3. In particular, in Fig. 10b, the first dissociation limit associated with the adiabatic dissociation in the ground state of the ion is the $CH_3^+ + I(^2P_{3/2})$ channel, while in the rigid case (Fig. 9b), the first dissociation limit was associated with the I^+ ion formation. Moreover, an interesting avoided crossing appears at $R_{C\text{-}I}$ around 3.8 Å in Fig. 10b. A similar avoided crossing was, in fact, predicted by Locht *et al.*[15] as well as by our group in a femtosecond photodissociation study using non resonant detection at 800 nm[47].

Although the symmetry of the electronic states cannot be deduced when we take into account the spin-orbit coupling in the calculations, the elements of the dipole moment matrix for the transition from the $CH_3I^+(\tilde{X}\,^2E_{3/2})$ to the different electronic states have been computed in the C_{3v} symmetry with the C-I bond along the *Z* axis. Inspection of the absolute values of the dipole moment for the three defined axis allows us to determine the parallel or perpendicular character of each transition. A larger value for the *Z* axis reflects a favoured transition when the C-I bond is parallel to the light polarization axis and, therefore, a parallel distribution is expected experimentally. On the other hand, large values on the *X* and/or *Y* axes highlight an expected perpendicular distribution. The transition to the slightly bounded first excited state, the so-called $\tilde{A}$ state, appears to be mostly perpendicular, as it was considered in previous reported work[10,15,17,18]. On the contrary, the manifold of repulsive states constituting the so-called $\tilde{B}$ state is composed of electronic states with different symmetry, while in the literature the $\tilde{B} \leftarrow \tilde{X}\,^2E$ transition is considered purely parallel. In particular, the transitions to the first repulsive states, represented by red dashed lines in Fig. 9b, are mostly characterized by a perpendicular orientation of the transition dipole moment while the transition to the repulsive state represented by an orange line is purely parallel.

Discussion

The measured angular and translational energy distributions can provide a picture of the dissociative ionization processes based on the PESs scheme and the symmetries deduced. CH_3I^+ ions in the $\tilde{X}\,^2E_{3/2}$ ground state are produced using a (2+1) REMPI scheme at 339.34 nm[22] through the $5p\pi \leftarrow 6p$ Rydberg state two-photon transition, which is characterized by a transition dipole moment parallel to the polarization axis. In the one-colour experiment, the absorption of a fourth 339.34 nm photon would lead to the $\tilde{A}^2A_1 \leftarrow \tilde{X}\,^2E$ excitation. Although this first state is slightly bound (see Figs. 9 and 10), the excess energy provided by the 339.34 nm photon should be enough to overcome the barrier. Figure 3 clearly shows that only contribution to the images for both fragments is the MPI dissociation process of the CH_3I^+ ion. The Boltzmann shapes of the associated TEDs (for all wavelengths studied in this work) result as a consequence of the fact that the energy provided by the photons is relaxed through internal couplings towards the lower excited states, where a CH_3I^+ ion highly ro-vibrationally excited is dissociated. The high anisotropy observed is a consequence of the strong molecular alignment produced by the four absorbed photons. The lack of a fast dissociation process through the $^2A_1$ state is explained due to the alignment of the CH_3I^+ ion along the intermolecular axis produced by the ionizing step. Since the transition dipole moment of the two-photon transition lies parallel to the C-I bond (parallel transition), the REMPI scheme used to produce the $CH_3I^+(\tilde{X}\,^2E_{3/2})$ ions generates, in turn, an ensemble of molecules with the C-I internuclear axis aligned along the light polarization direction. The $\tilde{A}^2A_1 \leftarrow \tilde{X}\,^2E$ transition possesses, on the other hand, perpendicular character, which means that the corresponding transition dipole moment is perpendicular to the C-I bond axis and, therefore, to the polarization vector of the fourth photon. The crossed orientation of both vectors reduces considerably – no signal is observed, actually – the probability of the absorption process.

In the two-colour experiments, the origin of the dissociative MPI anisotropic signal appearing in the centre of the images do not differ from that of the one colour experiment. Regarding the observed recoiled structures, the mechanism is clearer. The $CH_3I^+(\tilde{X}\,^2E_{3/2})$ ions formed in the first step by the three-photon absorption at 339.34 nm are later excited by the dissociation pulse to the so-called $\tilde{B}$ manifold of states, a manifold of pure repulsive states, as observed in Fig. 10b, leading to direct dissociation of CH_3I^+ into the $CH_3^+(\tilde{X}\,^1A_1') + I(^2P_{1/2})$ or $CH_3 + I^+(^3P_2)$ channels. Tentatively, and bearing in mind that the position of the computed electronic states of the ion at the Franck-Condon region is not highly accurate, the dissociation laser pulse could lead to the population of the excited state represented by the orange line in Fig. 10b. The transition to this state from the $CH_3I^+(\tilde{X}\,^2E_{3/2})$ ion is characterized by a parallel dipole moment in agreement with the measured angular distributions. In addition, this excited state correlates adiabatically with the $CH_3^+(\tilde{X}\,^1A_1') + I(^2P_{1/2})$ channel and no-adiabatically with the

$CH_3 + I^+(^3P_2)$ channel through an avoided crossing, observed at $R_{C\text{-}I}$=3.8 Å in Fig. 10b. Such mechanism would explain the anisotropic structures observed in the images of the CH_3^+ and I^+ ions. The experimental TEDs show a narrow structure located at the expected maximum available energy for these channels in agreement with a direct and rapid dissociation process. A possible vibrational excitation in the ν_3 mode, the symmetric C-I stretch, of the $CH_3I^+(\tilde{X}\,^2E_{3/2})$ ions may favour the dissociation process – without ruling out the participation of other less energetic modes – and in particular the $CH_3 + I^+(^3P_2)$ channel through the crossing. The participation of CH_3I^+ *hot bands* would explain the broader structures observed for the I^+ ion compared to those obtained for the CH_3^+ ion. At the lower dissociation energy corresponding to 260 nm, the $CH_3 + I^+(^3P_2)$ channel is not observed experimentally, suggesting that the excitation energy might not be enough to allow the transfer of population in the avoided crossing.

Conclusions

The one-colour and two-colour photodissociation dynamics of the CH_3I^+ cation have been studied using the velocity map imaging technique and nanosecond laser pulses. A first laser pulse is used to ionize CH_3I via a (2+1) REMPI scheme through the $5p\pi \leftarrow 6p$ Rydberg state two-photon transition. The $CH_3I^+(\tilde{X}\,^2E_{3/2})$ ions produced are subsequently excited at several wavelengths. The reported translational energy distributions for the CH_3^+ and I^+ ions highlight two different dissociation processes, characterized by a Boltzmann-type unstructured distribution at low energies as well as a recoiled narrow structure at higher energies. In addition, the measured angular distributions show a large alignment of the C-I bond of the molecule along the light polarization axis associated with both processes.

High level *ab initio* calculations have been performed in order to get a deeper understanding of the photodissociation dynamics of the CH_3I^+ ion. Direct dissociation of a repulsive state from the manifold of excited states representing the $\tilde{B}$ excited states manifold leads to the $CH_3^+(\tilde{X}\,^1A_1') + I(^2P_{1/2})$ formation while the $CH_3 + I^+(^3P_2)$ channel is populated through an avoided crossing outside the Franck-Condon region. The available energy is, therefore, totally converted into translational energy and, thus, a recoiled narrow structure characterizes this fast and direct dissociation process. On the contrary, an indirect process involving energy relaxation from highly excited electronic sates to the ground state is the most probable responsible of the observed Boltzmann-type distributions.

Further experiments on the photodissociation of the CH_3I^+ cation using an electron-ion coincidence technique could permit to get a deeper understanding of the dissociation mechanisms.

Acknowledgements

S.M.P. is grateful for the PICATA-Técnicos contract from the Campus de Excelencia Internacional Moncloa and LASING S.A. D. V. C. acknowledges a contract from MINECO under the Fondo de Garantía Juvenil. This work has been financed by the Spanish MINECO (grants CTQ2012-37404-C02-01 and CTQ2015-65033-P). The facilities provided by the Center for Ultrasfast Lasers of Universidad Complutense de Madrid are acknowledged.

Notes and references

1 D. W. Chandler, J. W. Thoman, M. H. M. Janssen and D. H. Parker, *Chem. Phys. Lett.*, 1989, **156**, 151–158.
2 A. T. J. B. Eppink and D. H. Parker, *J. Chem. Phys.*, 1998, **109**, 4758–4767.
3 A. T. J. B. Eppink and D. H. Parker, *J. Chem. Phys.*, 1999, **110**, 832–844.
4 L. Rubio-Lago, A. García-Vela, A. Arregui, G. A. Amaral and L. Bañares, *J. Chem. Phys.*, 2009, **131**, 174309.
5 M. G. González, J. D. Rodríguez, L. Rubio-Lago, A. García-Vela and L. Bañares, *Phys. Chem. Chem. Phys.*, 2011, **13**, 16404–16415.
6 D. W. Chandler and P. L. Houston, *J. Chem. Phys.*, 1987, **87**, 1445–1447.
7 A. T. Eppink and D. H. Parker, *Rev. Sci. Instrum.*, 1997, **68**, 3477–3484.
8 L. Karlsson, R. Jadrny, L. Mattsson, F. T. Chau and K. Siegbahn, *Phys. Scr.*, 1977, **16**, 225.
9 W. von Niessen, L. Åsbrink and G. Bieri, *J. Electron Spectrosc. Relat. Phenom.*, 1982, **26**, 173–201.
10 D. M. P. Holland, I. Powis, G. Öhrwall, L. Karlsson and W. von Niessen, *Chem. Phys.*, 2006, **326**, 535–550.
11 Y. J. Bae and M. S. Kim, *ChemPhysChem*, 2008, **9**, 1709–1714.
12 M. Lee and M. S. Kim, *J. Chem. Phys.*, 2007, **126**, 154317.
13 Y. J. Bae and M. S. Kim, *J. Chem. Phys.*, 2008, **128**, 124324.
14 M. Grütter, J. M. Michaud and F. Merkt, *J. Chem. Phys.*, 2011, **134**, 054308.
15 R. Locht, D. Dehareng, K. Hottmann, H. W. Jochims, H. Baumgärtel and B. Leyh, *J. Phys. B At. Mol. Opt. Phys.*, 2010, **43**, 105101.
16 Y. Wang, S. Zhang, Z. Wei and B. Zhang, *J. Phys. Chem. A*, 2008, **112**, 3846–3851.
17 F. Aguirre, S. T. Pratt and others, *J. Chem. Phys.*, 2003, **118**, 6318–6326.
18 F. Aguirre and S. T. Pratt, *J. Chem. Phys.*, 2003, **119**, 9476–9485.
19 V. Blanchet, P. C. Samartzis and A. M. Wodtke, *J. Chem. Phys.*, 2009, **130**, 034304.
20 F. Wang, M. L. Lipciuc, X. Yang and T. N. Kitsopoulos, *Phys. Chem. Chem. Phys.*, 2009, **11**, 2234–2240.
21 S. H. Gardiner, T. N. Karsili, M. L. Lipciuc, E. Wilman, M. N. Ashfold and C. Vallance, *Phys. Chem. Chem. Phys.*, 2014, **16**, 2167–2178.
22 M. R. Dobber, W. J. Buma and C. A. De Lange, *J. Chem. Phys.*, 1993, **99**, 836–853.
23 V. Papadakis and T. N. Kitsopoulos, *Rev. Sci. Instrum.*, 2006, **77**, 083101.
24 L. Rubio-Lago, G. A. Amaral, A. N. Oldani, J. D. Rodríguez, M. G. González, G. A. Pino and L. Bañares, *Phys. Chem. Chem. Phys.*, 2011, **13**, 1082–1091.

25 P.-O. Widmark, P.-Å. Malmqvist and B. O. Roos, *Theor. Chem. Acc. Theory Comput. Model. Theor. Chim. Acta*, 1990, **77**, 291–306.
26 B. O. Roos, R. Lindh, P.-Å. Malmqvist, V. Veryazov and P.-O. Widmark, *J. Phys. Chem. A*, 2004, **108**, 2851–2858.
27 B. Schimmelpfennig, 1996.
28 H.-J. Werner, P. J. Knowles, R. Lindh, F. R. Manby, M. Schütz, P. Celani, T. Korona, A. Mitrushenkov, G. Rauhut, T. B. Adler, R. D. Amos, A. Bernhardsson, A. Berning, D. L. Cooper, M. J. O. Deegan, A. J. Dobbyn, F. Eckert, E. Goll, C. Hampel, G. Hetzer, T. Hrenar, G. Knizia, C. Köppl, Y. Liu, A. W. Lloyd, R. A. Mata, A. J. May, S. J. McNicholas, W. Meyer, M. E. Mura, A. Nicklass, P. Palmieri, K. Pflüger, R. Pitzer, M. Reiher, U. Schumann, H. Stoll, A. J. Stone, R. Tarroni, T. Thorsteinsson, M. Wang and A. Wolf, *MOLPRO, version 2012*.
29 H.-J. Werner, P. J. Knowles, G. Knizia, F. R. Manby and M. Schütz, *Wiley Interdiscip. Rev. Comput. Mol. Sci.*, 2012, **2**, 242–253.
30 R. Lindh, U. Ryu and B. Liu, *J. Chem. Phys.*, 1991, **95**, 5889–5897.
31 H.-J. Werner and P. J. Knowles, *J. Chem. Phys.*, 1985, **82**, 5053–5063.
32 P. J. Knowles and H.-J. Werner, *Chem. Phys. Lett.*, 1985, **115**, 259–267.
33 P. J. Knowles and H.-J. Werner, *Theor. Chim. Acta*, **84**, 95–103.
34 H.-J. Werner and P. J. Knowles, *J. Chem. Phys.*, 1988, **89**, 5803–5814.
35 P. J. Knowles and H.-J. Werner, *Chem. Phys. Lett.*, 1988, **145**, 514–522.
36 K. R. Shamasundar, G. Knizia and H.-J. Werner, *J. Chem. Phys.*, 2011, **135**, 054101.
37 F. Eckert, P. Pulay and H.-J. Werner, *J. Comput. Chem.*, 1997, **18**, 1473–1483.
38 A. E. Azhary, G. Rauhut, P. Pulay and H.-J. Werner, *J. Chem. Phys.*, 1998, **108**, 5185–5193.
39 P. Celani and H.-J. Werner, *J. Chem. Phys.*, 2003, **119**, 5044–5057.
40 M. Reiher and A. Wolf, *J. Chem. Phys.*, 2004, **121**, 2037.
41 M. Reiher and A. Wolf, *J. Chem. Phys.*, 2004, **121**, 10945.
42 D. Peng and M. Reiher, *Theor. Chem. Acc.*, 2012, **131**, 1081.
43 A. Berning, M. Schweizer, H.-J. Werner, P. J. Knowles and P. Palmieri, *Mol. Phys.*, 2000, **98**, 1823–1833.
44 T. A. Carlson, P. Gerard, B. P. Pullen and F. A. Grimm, *J. Chem. Phys.*, 1988, **89**, 1464–1468.
45 R. N. Dixon, *J. Chem. Phys.*, 2005, **122**.
46 C. Elkharrat, Y. J. Picard, P. Billaud, C. Cornaggia, D. Garzella, M. Perdrix, J. C. Houver, R. R. Lucchese and D. Dowek, *J. Phys. Chem. A*, 2010, **114**, 13288–13288.
47 J. Durá, R. de Nalda, G. A. Amaral and L. Bañares, *J. Chem. Phys.*, 2009, **131**, 134311.

TABLES

Table 1. Energy at the Franck-Condon (FC) geometry as well as at the dissociation limit for calculated electronic states with respect to the CH_3I ($\tilde{X}\,A_1$) ground state.

State number	FC geometry	Dissociation energy, E_D (eV)	Dissociation Limit
1	9.10	12.12	$CH_3^+ + I(^2P_{3/2})$
2	9.10	12.12	
3	9.78	12.13	
4	9.78	12.13	
5	12.37	12.30	$I^+(^3P_2) + CH_3$
6	12.37	12.30	
7	14.43	12.30	
8	14.43	12.30	
9	14.57	12.30	
10	14.57	12.30	
11	15.23	12.30	
12	15.23	12.30	
13	15.31	12.30	
14	15.31	12.30	
15	15.63	13.15	$CH_3^+ + I(^2P_{1/2})$
16	15.63	13.15	
17	16.12	13.16	$I^+(^3P_0)+CH_3$
18	16.12	13.16	
19	16.22	13.23	$I^+(^3P_1)+CH_3$
20	16.22	13.23	
21	16.26	13.23	
22	16.26	13.23	
23	16.31	13.23	
24	16.31	13.23	
25	17.03	14.15	$I^+(^1D_0)+CH_3$
26	17.03	14.15	
27	17.32	14.15	
28	17.32	14.15	
29	17.48	14.15	
30	17.48	14.15	
31	19.46	14.15	
32	19.46	14.15	
33	20.24	14.15	
34	20.24	14.15	
35	21.29	16.21	$I^+(^1S) + CH_3$
36	21.29	16.21	

Table 2. β anisotropy parameters obtained from the fit of the angular distributions presented in Figures 7 and 8.

	$CH_3^+ + I^*(^2P_{1/2})$			$CH_3 + I^+(^3P_2)$		
λ_{dis} (nm)	β_2	β_4	β_6	β_2	β_4	β_6
339	1.84	0.12	-	1.50	0.65	0.25
260	1.53	-0.43	-	-	-	-
250	1.54	-0.47		2.30	0.40	-0.04
242	1.67	-0.33	-	2.66	0.88	-0.14

Table 3. Calculated dissociation limits, considering the methyl moiety with a rigid pyramidal geometry or the relaxation of this radical to a planar geometry, with respect to the $CH_3I^+(\tilde{X}\,^2E_{3/2})$ energy compared to those from the literature.

Products	Dissociation energy, E_D (eV)			
	This Work		Literature	
	Without relax	Relax		
$\mathbf{CH_3^+} + I(^2P_{3/2})$	3.85	3.00	2.45 [Ref. 15]	2.64 [Ref. 16]
$CH_3 + \mathbf{I^+}(^3P_2)$	3.33	3.18	3.05 [Ref. 15]	3.36 [Ref. 16]
$\mathbf{CH_3^+} + I(^2P_{1/2})$	4.88	4.03		3.67 [Ref. 16]
$CH_3 + \mathbf{I^+}(^3P_0)$	4.20	4.03		
$CH_3 + \mathbf{I^+}(^3P_1)$	4.26	4.10		
$CH_3 + \mathbf{I^+}(^1D_0)$	5.18	5.03		
$CH_3 + \mathbf{I^+}(^1S)$	7.43	7.09		

FIGURE CAPTIONS

Fig. 1 Scheme of the experimental procedure. A first laser pulse centred at 339.34 nm is used to produce methyl iodine cations in a (2+1) REMPI scheme *via* a two-photon resonant excitation to the 6*p* Rydberg state. The CH_3I^+ ions in the ground state are excited by a second laser pulse at wavelengths between 339 and 242 nm. The I^+ and CH_3^+ fragments produced are detected by velocity map imaging.

Fig. 2 Orbitals contained in the selected active space calculation CAS(5,4) at Frank-Condon geometry.

Fig. 3 (a,c) Abel inverted velocity map images for CH_3^+ (a) and I^+ (b) ions from the methyl iodide photoexcitation in a one-colour experiment at 339.34 nm. (b,d) Corresponding translational energy distributions obtained from the angular integration of the inverted images (a,c).

Fig. 4 (a,c) Abel inverted velocity map images for CH_3^+ (a) and I^+ (b) ions from the methyl iodide photoexcitation in a two-colour experiment at 339.34 nm and 260 nm. (b,d) Translational energy distributions obtained from the angular integration of the inverted images (a,c). In (b), the region of interest is presented in detail while the inset shows the complete distribution.

Fig. 5 (a,c) Abel inverted velocity map images for CH_3^+ (a) and I^+ (b) ions from the methyl iodide photoexcitation in a two-colour experiment at 339.34 nm and 250 nm. (b, d) Translational energy distributions obtained from the angular integration of the inverted images (a, c).

Fig. 6 (a, c) Abel inverted velocity map images for CH_3^+ (a) and I^+ (b) ions from the methyl iodide photoexcitation in a two-colour experiment at 339.34 nm and 242 nm. (b, d) Translational energy distributions obtained from the angular integration of the inverted images (a, c).

Fig. 7 Angular distributions for CH_3^+ ions from the methyl iodide photoexcitation at 339.34 nm (a) and in two-colour experiments at 339.34 nm and 260 nm (b), 250 nm (c) and 242 nm (d), obtained from the radial integration of the inverted images in Fig 3a, Fig 4a, Fig 5a and Fig. 6a, respectively. Open circles: experimental points. Solid line: fit to equation (6).

Fig. 8 Angular distributions for I^+ ions from the methyl iodide photoexcitation at 339.34 nm (a), and in a two-colour experiment at 339.34 nm and 250 nm (b) and 242 nm (c), obtained from the radial integration of the inverted images in Fig 3(c), Fig 5(c) and Fig. 6(c), respectively. Open circles: experimental points. Solid line: fit to equation (6).

Fig. 9 Computed CASSCF potential energy surfaces for the methyl iodide cation considering a rigid pyramidal geometry of the methyl moiety.

Fig. 10 Computed CASSCF potential energy surfaces for the methyl iodide cation considering a relaxed planar geometry of the methyl moiety.

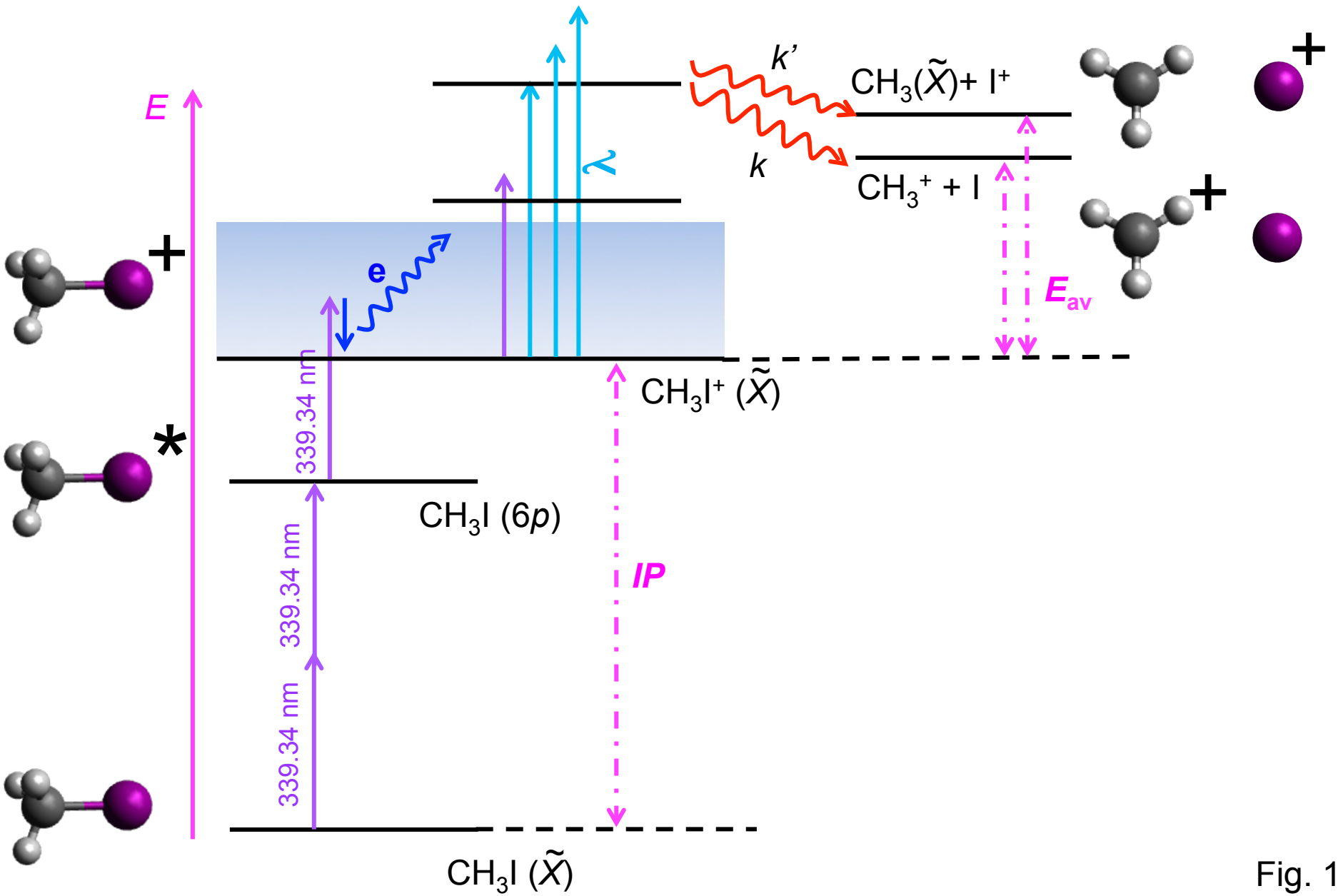
E
+
*
e
339.34 nm
339.34 nm
339.34 nm
CH3I (6p)
CH3I+ (X̃)
IP
CH3I (X̃)
k'
k
CH3(X̃)+ I+
CH3+ + I
Eav

Fig. 1

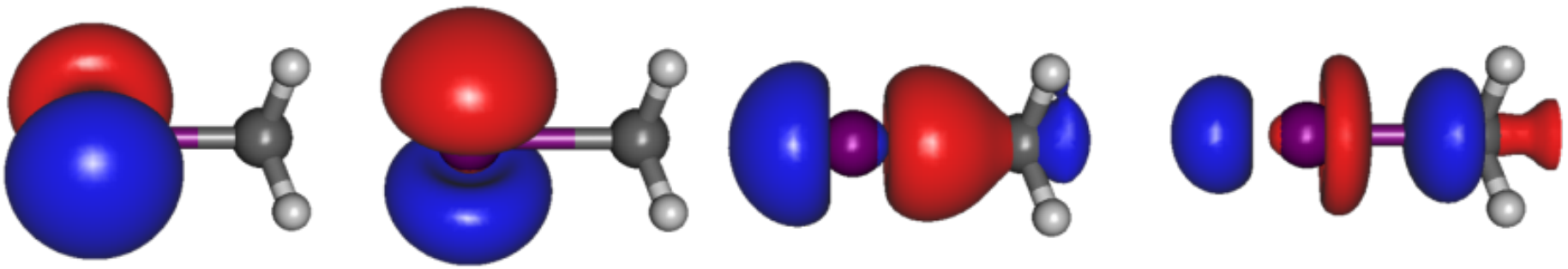

Fig. 2

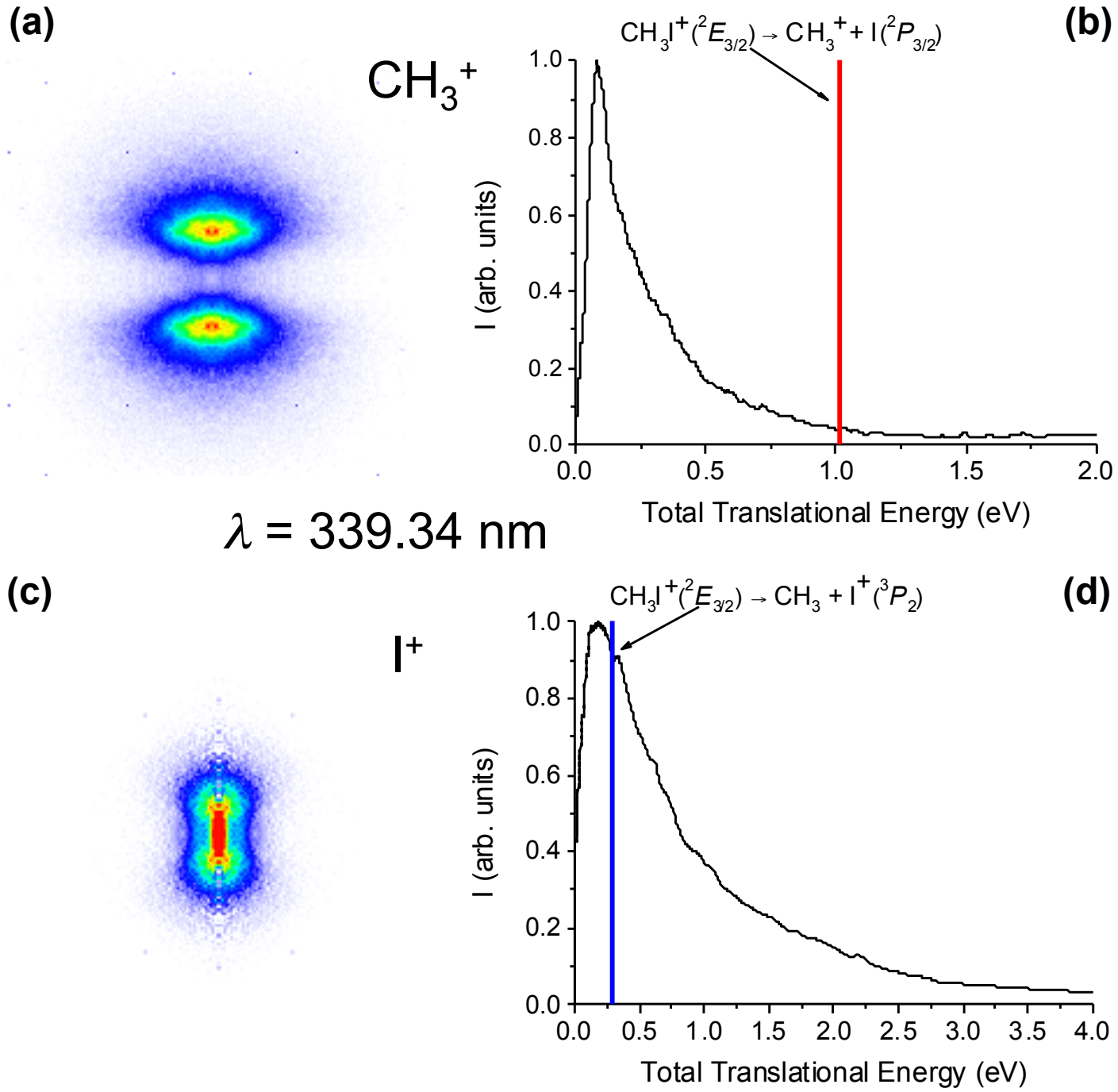
(a)
CH_3^+
(b)
$CH_3I^+(^2E_{3/2}) \rightarrow CH_3^+ + I(^2P_{3/2})$
I (arb. units)
Total Translational Energy (eV)
λ = 339.34 nm
(c)
I^+
(d)
$CH_3I^+(^2E_{3/2}) \rightarrow CH_3 + I^+(^3P_2)$
I (arb. units)
Total Translational Energy (eV)

Fig. 3

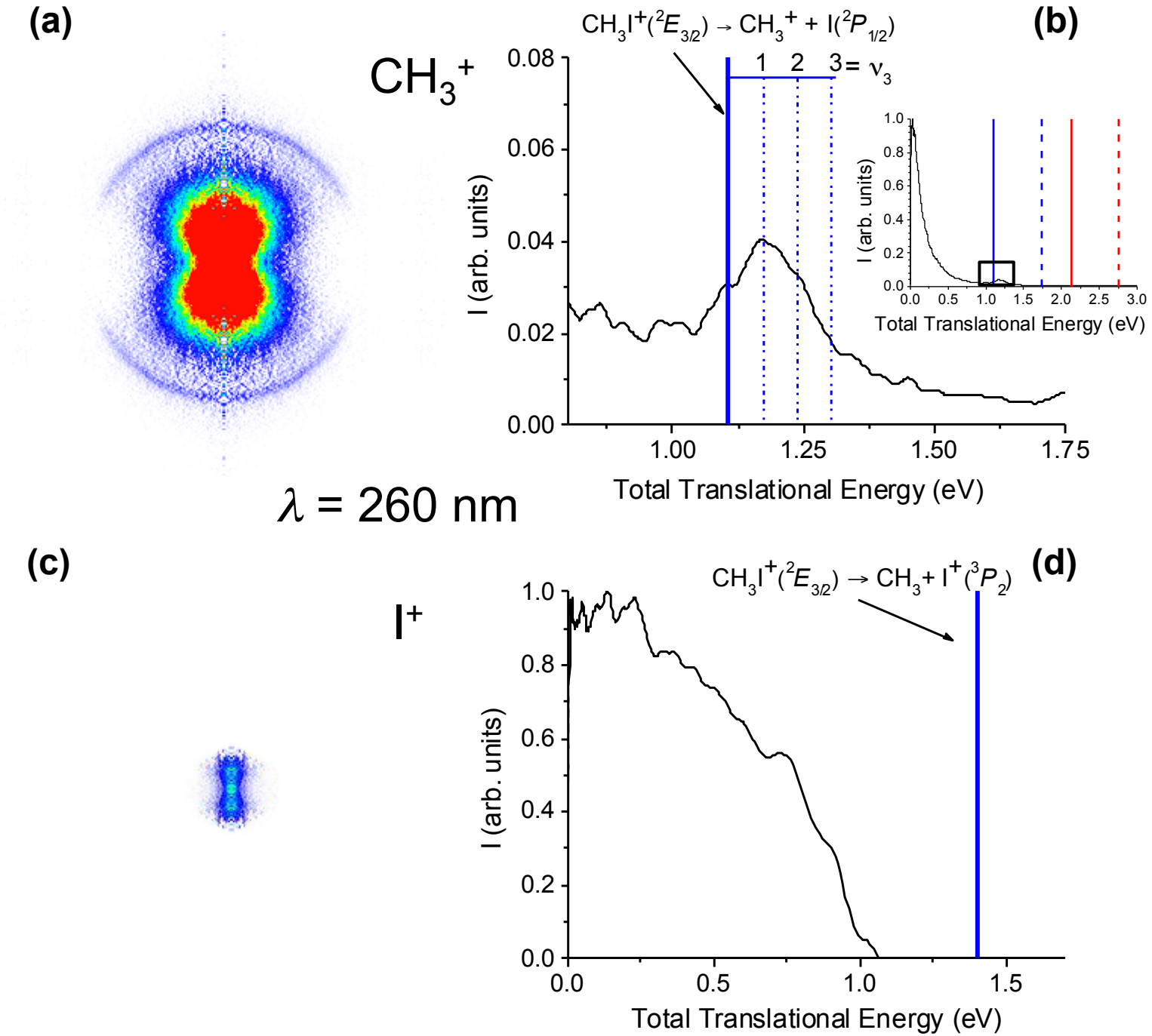
(a)
CH_3^+
(b)
$CH_3I^+(^2E_{3/2}) \rightarrow CH_3^+ + I(^2P_{1/2})$
1 2 3= ν_3
I (arb. units)
Total Translational Energy (eV)
λ = 260 nm
(c)
I^+
(d)
$CH_3I^+(^2E_{3/2}) \rightarrow CH_3 + I^+(^3P_2)$
I (arb. units)
Total Translational Energy (eV)

Fig. 4

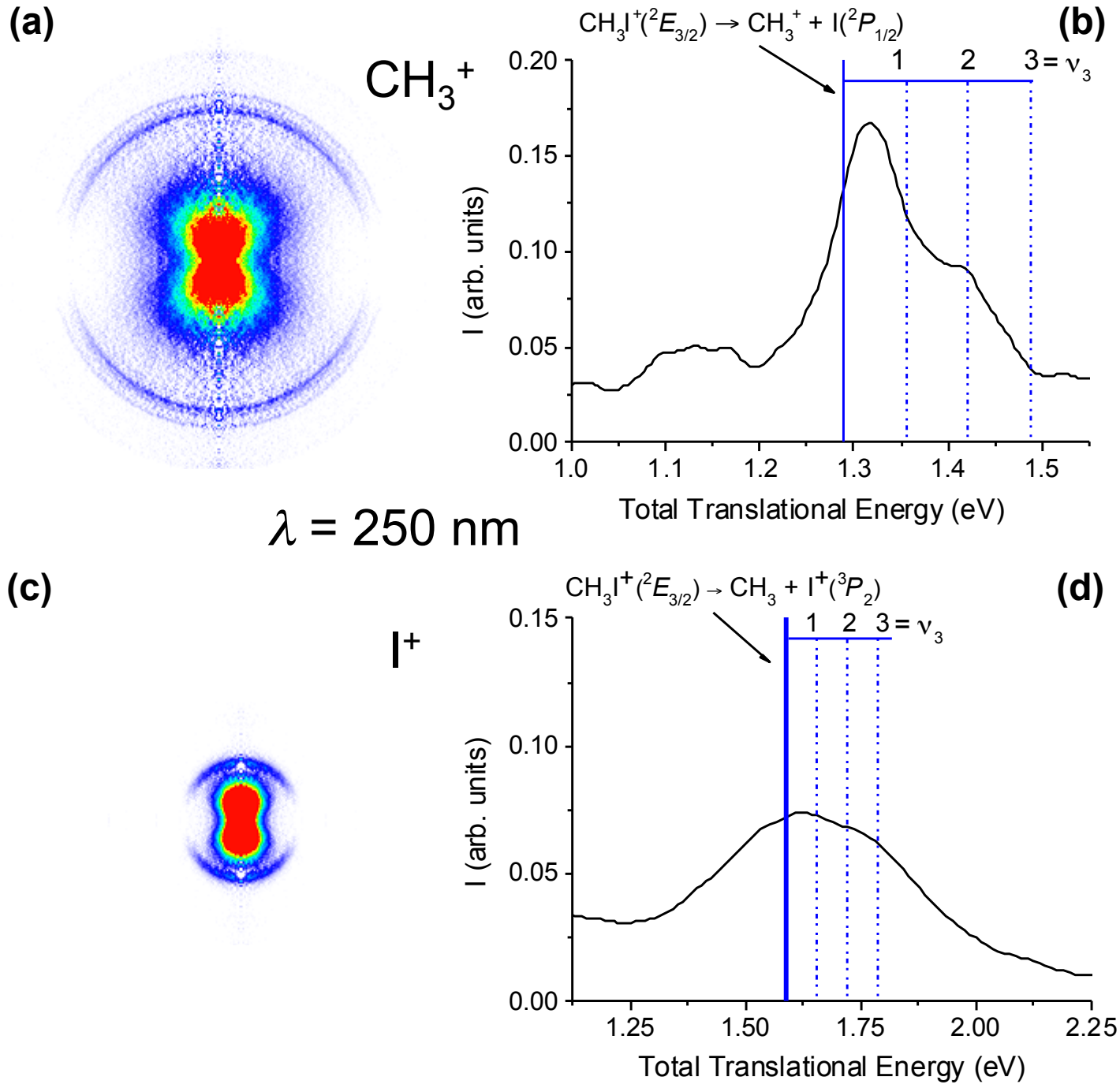
(a)
CH_3^+
(b)
$CH_3I^+(^2E_{3/2}) \rightarrow CH_3^+ + I(^2P_{1/2})$
1
2
3 = ν_3
0.20
0.15
0.10
0.05
0.00
I (arb. units)
1.0
1.1
1.2
1.3
1.4
1.5
Total Translational Energy (eV)
λ = 250 nm
(c)
I^+
(d)
$CH_3I^+(^2E_{3/2}) \rightarrow CH_3 + I^+(^3P_2)$
1
2
3 = ν_3
0.15
0.10
0.05
0.00
I (arb. units)
1.25
1.50
1.75
2.00
2.25
Total Translational Energy (eV)

Fig. 5

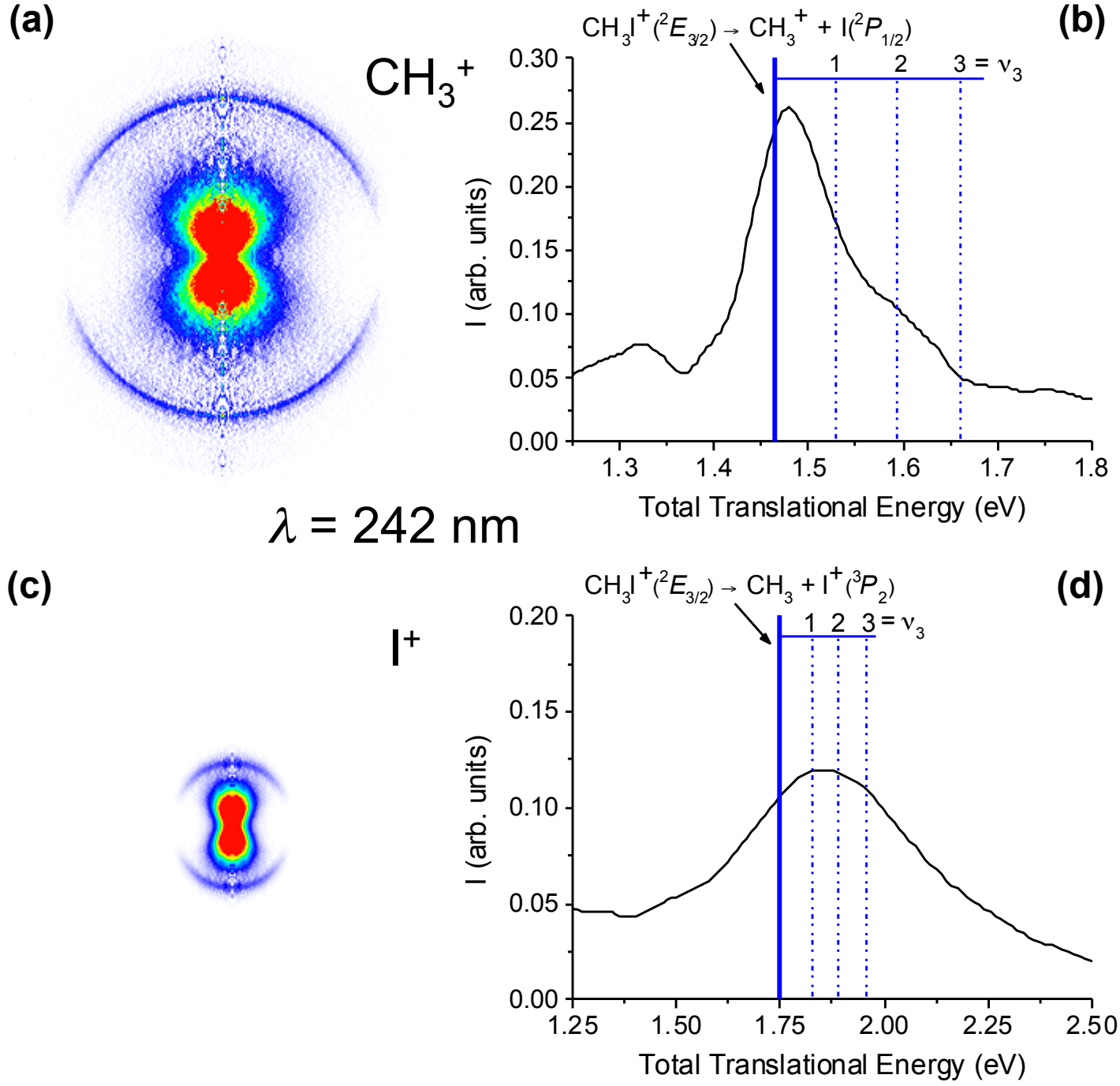
(a)
CH_3^+
(b)
$CH_3I^+(^2E_{3/2}) \rightarrow CH_3^+ + I(^2P_{1/2})$
1
2
3 = ν_3
I (arb. units)
Total Translational Energy (eV)
λ = 242 nm
(c)
I^+
(d)
$CH_3I^+(^2E_{3/2}) \rightarrow CH_3 + I^+(^3P_2)$
1 2 3 = ν_3
I (arb. units)
Total Translational Energy (eV)

Fig. 6

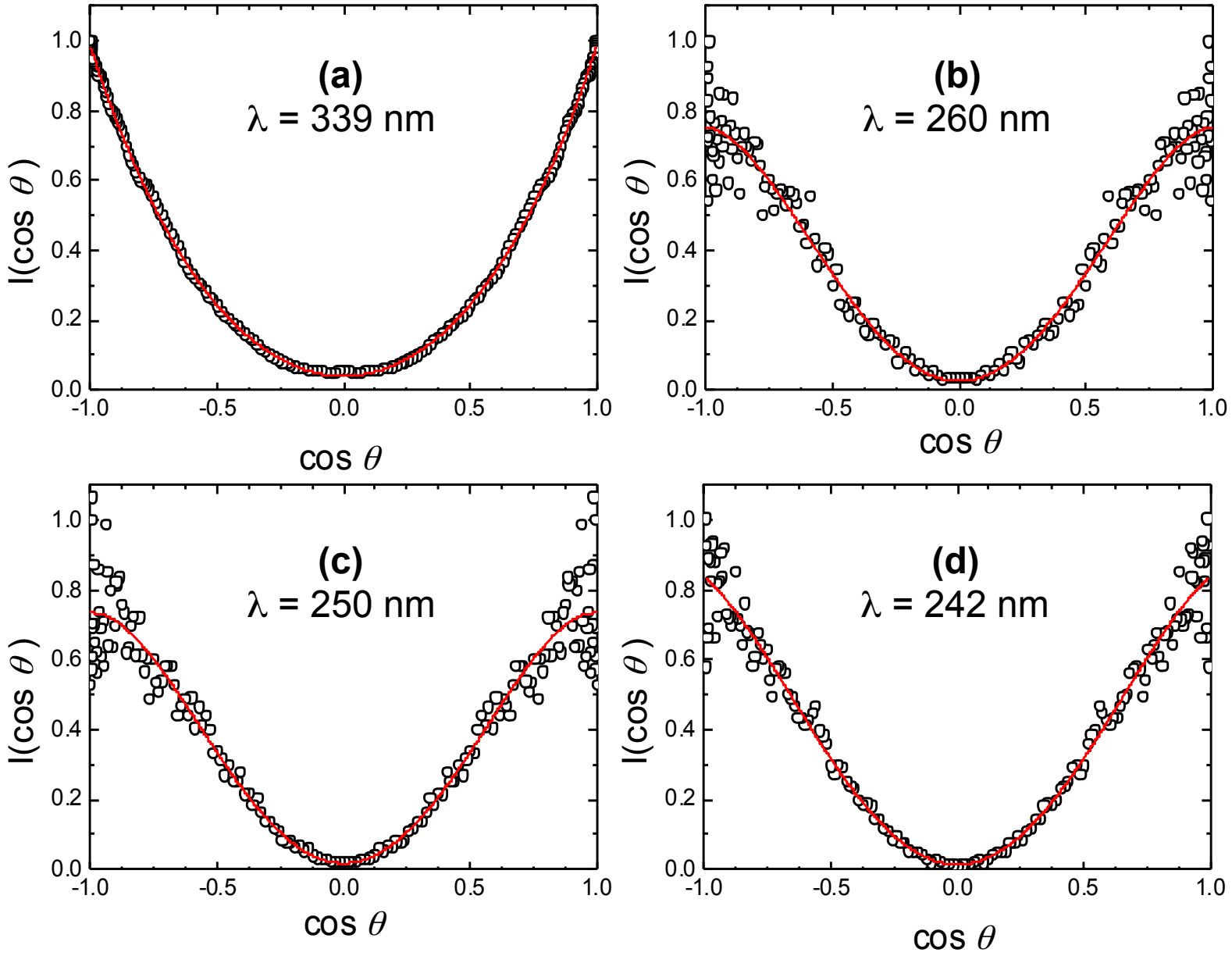
(a)
λ = 339 nm
(b)
λ = 260 nm
(c)
λ = 250 nm
(d)
λ = 242 nm
I(cos θ)
cos θ
1.0
0.8
0.6
0.4
0.2
0.0
-1.0
-0.5
0.0
0.5
1.0

Fig. 7

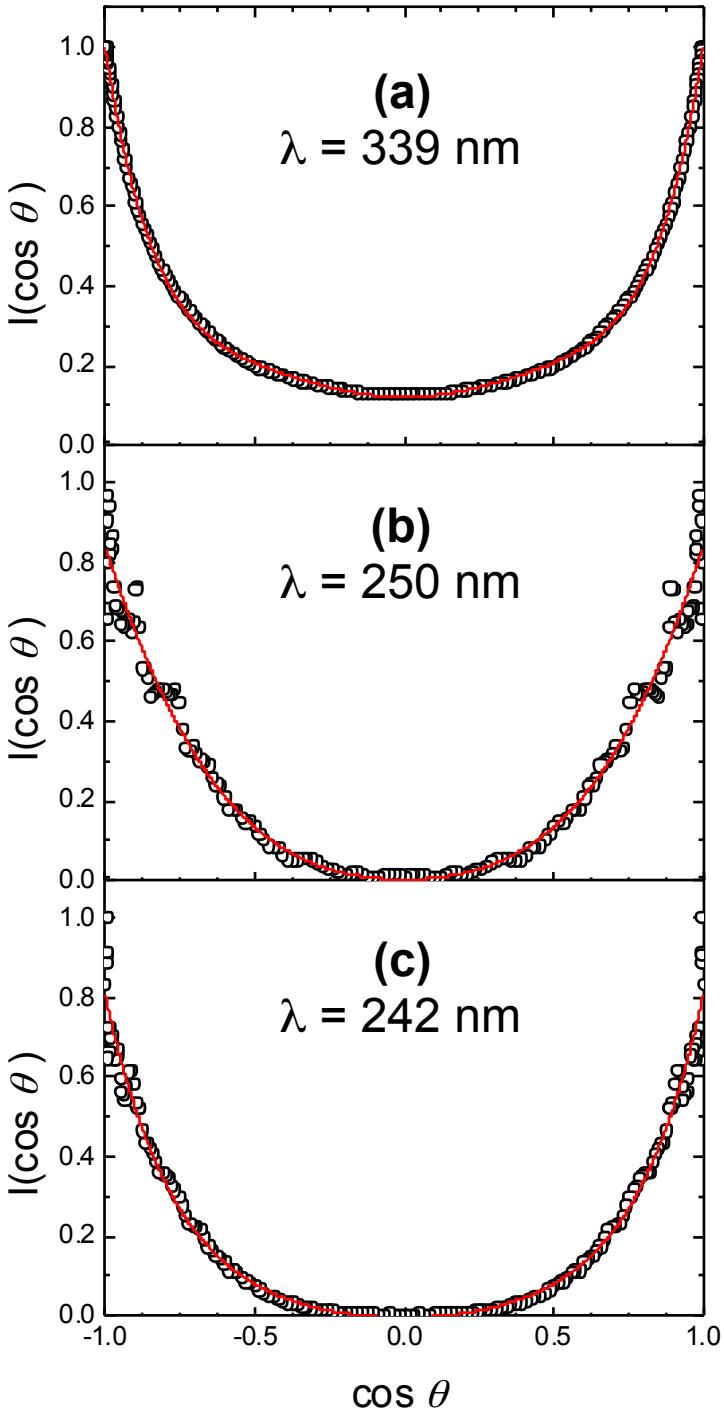
(a)
λ = 339 nm
(b)
λ = 250 nm
(c)
λ = 242 nm
I(cos θ)
cos θ
1.0
0.8
0.6
0.4
0.2
0.0
-1.0
-0.5
0.0
0.5
1.0

Fig. 8

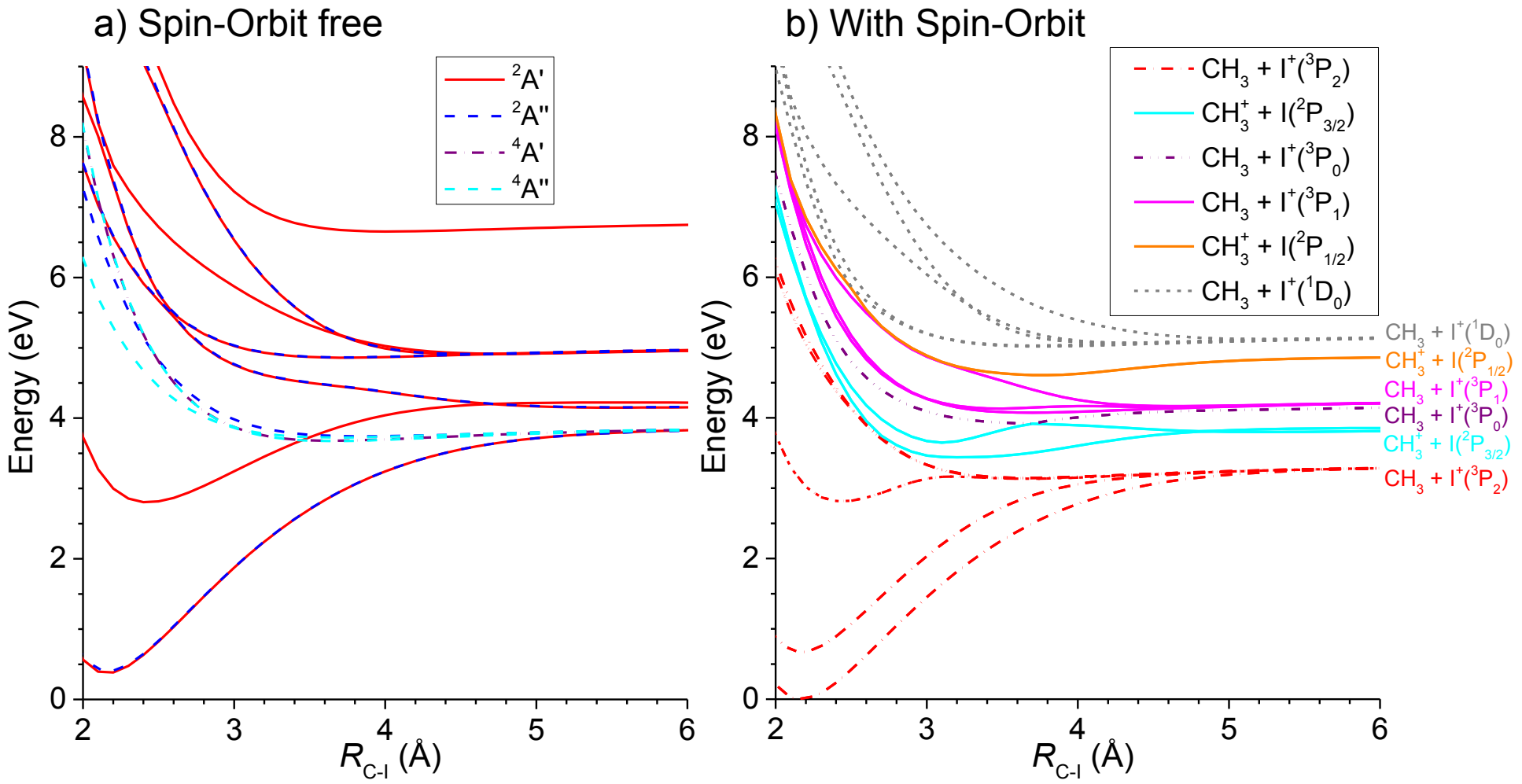
a) Spin-Orbit free
b) With Spin-Orbit
Energy (eV)
R_{C-I} (Å)
$^2A'$
$^2A''$
$^4A'$
$^4A''$
$CH_3 + I^+(^3P_2)$
$CH_3^+ + I(^2P_{3/2})$
$CH_3 + I^+(^3P_0)$
$CH_3 + I^+(^3P_1)$
$CH_3^+ + I(^2P_{1/2})$
$CH_3 + I^+(^1D_0)$

Fig. 9

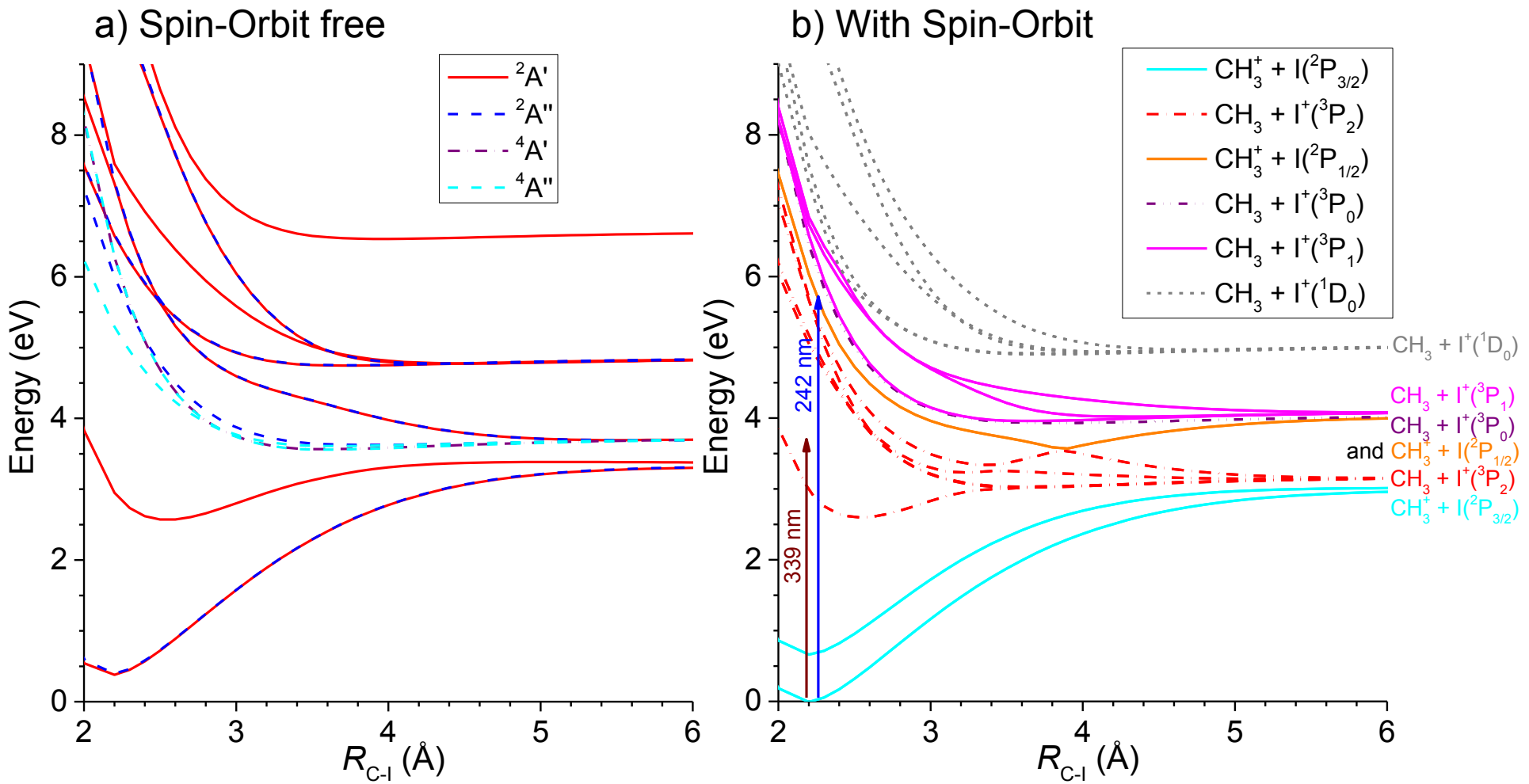
a) Spin-Orbit free
b) With Spin-Orbit
Energy (eV)
$R_{C\text{-}I}$ (Å)
^{2}A'
^{2}A''
^{4}A'
^{4}A''
$CH_3^+ + I(^2P_{3/2})$
$CH_3 + I^+(^3P_2)$
$CH_3^+ + I(^2P_{1/2})$
$CH_3 + I^+(^3P_0)$
$CH_3 + I^+(^3P_1)$
$CH_3 + I^+(^1D_0)$
242 nm
339 nm
and

Fig. 10